

# Indoor Synthetic Aperture Radar Measurements of Point-Like Targets Using a Wheeled Mobile Robot

Yuma E. Ritterbusch<sup>a</sup>, Johannes Fink<sup>a</sup>, and Christian Waldschmidt<sup>b</sup>

<sup>a</sup>Robert Bosch GmbH, Corporate Sector Research and Advance Engineering, 71272 Renningen, Germany

<sup>b</sup>Institute of Microwave Engineering, Ulm University, 89081 Ulm, Germany

## Abstract

Small, low-cost radar sensors offer a lighting independent sensing capability for indoor mobile robots that is useful for localization and mapping. Synthetic aperture radar (SAR) offers an attractive way to increase the angular resolution of small radar sensors for use on mobile robots to generate high-resolution maps of the indoor environment. This work quantifies the maximum synthesizable aperture length of our mobile robot measurement setup using radar-inertial odometry localization and offers insights into challenges for robotic millimeter-wave SAR imaging.

## 1 Introduction

Low-cost automotive radar sensors have been successfully applied in mobile robotics research to aid in indoor and outdoor navigation using radar-inertial odometry (RIO) [1]. These sensors have also been used for simultaneous localization and mapping (SLAM) based on radar point clouds created using digital beamforming (DBF) [2]. The achievable angular resolution of DBF is directly related to the physical extent of the multiple-input multiple-output (MIMO) antenna aperture of the sensor. The physical antenna aperture size can only be increased by designing a larger sensor with many channels, thus increasing manufacturing costs and power consumption. SAR imaging techniques offer an attractive digital signal processing alternative to achieve high angular resolution using a small antenna aperture with only a few channels. SAR processing has previously been applied in the automotive context to image the driving environment [3]. Another key benefit of the coherent processing of multiple radar measurements is an improvement of signal-to-noise ratio (SNR) in the image which can help to identify objects with smaller radar cross-section (RCS) and improve the accuracy of high-resolution probabilistic maps in an automotive setting [4]. Our focus is to bring the benefits of SAR imaging to the field of mobile robotics in indoor scenarios. Indoor mobile robots need to perform localization without relying on highly accurate external reference systems such as a global navigation satellite system (GNSS), which limits the accuracy of the estimated robot trajectory. Furthermore radar-inertial sensor fusion approaches [1] rely on odometry measurements only and hence suffer from the trajectory estimate drifting away from the ground truth over time. This imperfect trajectory estimate presents a key limiting factor to the maximum achievable synthetic aperture length. This paper aims to quantify this limitation in our experimental setup shown in **figure 1**. To this end we analyze the achieved cross-range resolution of SAR images computed

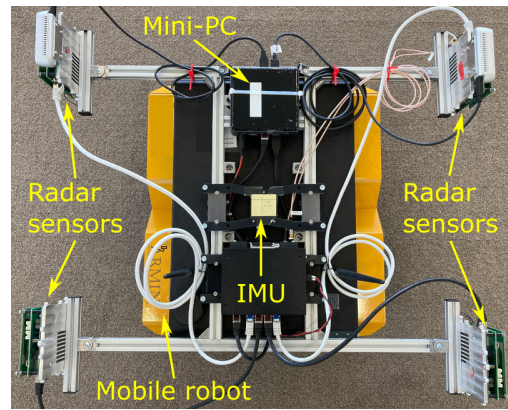


**Figure 1** Remote-controlled mobile robot with radar sensors, IMU and mini-PC for data recording.

based on a radar-inertial odometry (RIO) trajectory estimate [1]. This contrasts with the contributions [3, 4, 5] which do not explicitly mention achieved SAR resolution for non-simulated datasets. The remainder of this paper is organized as follows. The system model and experimental setup are described in sections 2 and 3 respectively. Results are presented and discussed in section 4 while section 5 provides a summary of the findings.

## 2 System model

### 2.1 Signal model

The radar sensors considered in this work use a chirp-sequence (CS) FMCW time-division multiplexing (TDM) MIMO modulation scheme, in which radar frames consisting of a sequence of  $N_c$  linear frequency chirps with duration  $T_c$  and bandwidth  $B$  are transmitted at a period  $T_f$ . During transmission of a frame, the time division multiplexing scheme cycles through  $N_T$  transmit channels at an interval  $T_T$  creating the interleaved transmit pattern shown in **figure 2**. The  $N_R$  receive channels are always

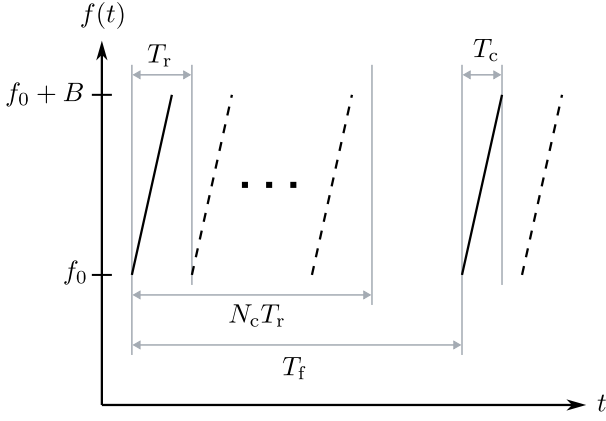


**Figure 2** Chirp-sequence FMCW TDM timing diagram for  $N_T = 2$  transmitters (solid and dashed lines).

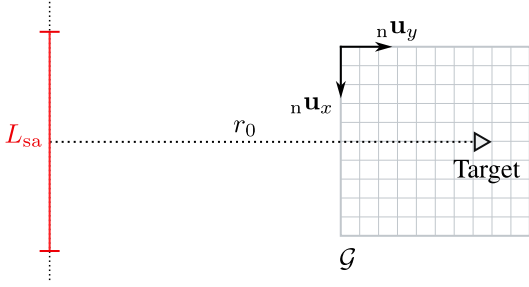


**Figure 3** Side-looking imaging geometry showing the synthetic aperture highlighted in red. The image grid surrounding the target of interest is defined by the basis vectors  ${}_n \mathbf{u}_x$  and  ${}_n \mathbf{u}_y$ .

active. Overall this results in  $N_T N_R$  virtual channels with  $N_c/N_T$  slow-time and  $T_c f_s$  fast-time samples available for baseband signal processing [6]. The equivalent complex baseband signal of a single point-target resulting from one chirp-sequence after downconversion and low-pass filtering is

$$\begin{aligned} \forall i \in [0, 1, \dots, N_T - 1], j \in [0, 1, \dots, N_R - 1], \\ n_s \in [0, 1, \dots, N_c/N_T - 1], n_f \in [0, 1, \dots, T_c f_s - 1] : \\ s_{ij}(n_s, n_f) = A_{ij} \exp \left\{ j \frac{2\pi}{c} \left( f_0 + \gamma \frac{n_f}{f_s} \right) r_{ij}(n_s, n_f) \right\} \end{aligned} \quad (1)$$

with amplitude  $A_{ij}$ , chirp-rate  $\gamma = B/T_c$ , and the propagation speed of electromagnetic waves  $c$  in the considered medium. The two-way target range for the pair of transmitter  $i$  and receiver  $j$  is

$$\begin{aligned} r_{ij}(n_s, n_f) = & \| {}_n \mathbf{p}_i(n_s, n_f) - {}_n \mathbf{p}_t \|_2 \\ & + \| {}_n \mathbf{p}_j(n_s, n_f) - {}_n \mathbf{p}_t \|_2, \end{aligned} \quad (2)$$

where the vectors  ${}_n \mathbf{p}_i, {}_n \mathbf{p}_j, {}_n \mathbf{p}_t \in \mathbb{R}^3$  denote the position vectors of transmit channel  $i$ , receive channel  $j$  and the target respectively, expressed in common reference frame  $n$ .  $\|\cdot\|_2$  denotes the Euclidean distance.

## 2.2 SAR image formation

The SAR images are computed using a time-domain back-projection (TDBP) algorithm [5], which first performs a

range-compression of the baseband signal by applying a window function  $w_r(n_f)$  for sidelobe control and DFT along the fast-time index  $n_f$  to obtain the range profiles

$$\begin{aligned} S_{ij}(n_s, r) &= \text{DFT} \{ w_r(n_f) s_{ij}(n_s, n_f) \} \\ &\approx A_{ij} \exp \left\{ j \frac{2\pi f_0}{c} r_{ij}(n_s) \right\} \\ &\quad \cdot W_r \left( \frac{2\pi\gamma}{c f_s} (r - r_{ij}(n_s)) \right), \end{aligned} \quad (3)$$

where the range-change during the short chirp duration  $T_c$  is assumed to be sufficiently small such that the fast-time index  $n_f$  in the exponential can be omitted.  $W_r(\Omega)$  is the DTFT of the window function  $w_r(n_f)$ .

The range-resolution after range-compression is [7]

$$\delta_r = \eta_r \frac{c}{2B}, \quad (4)$$

with the window-dependent main lobe-broadening factor  $\eta_r$ . The second step of SAR image formation is the azimuth-compression. The complex amplitudes of each range profile  $S_{ij}(n_s, r)$  are interpolated onto an image grid  $\mathcal{G} \subset \mathbb{R}^3$  and a matched filter

$$H(r) = \exp \left\{ -j \frac{2\pi f_0}{c} r \right\} \quad (5)$$

is applied for every grid point. Finally all available range-profile samples are coherently integrated to yield the image

$$I(\mathcal{G}) = \sum_{i=0}^{N_T-1} \sum_{j=0}^{N_R-1} \sum_{n_s=0}^{\frac{N_c}{N_T}-1} S_{ij}(n_s, \tilde{r}_{ij}(n_s)) H(\tilde{r}_{ij}(n_s)), \quad (6)$$

where

$$\begin{aligned} \forall {}_n \mathbf{g} \in \mathcal{G} : \quad \tilde{r}_{ij}(n_s) = & \| {}_n \mathbf{p}_i(n_s) - {}_n \mathbf{g} \|_2 \\ & + \| {}_n \mathbf{p}_j(n_s) - {}_n \mathbf{g} \|_2 \end{aligned} \quad (7)$$

is the two-way range from each transmitter/receiver pair  $ij$  to every point in the image grid. **Figure 3** shows the SAR imaging geometry for a synthetic aperture of length  $L_{sa}$  and a range of closest approach to the target  $r_0$ . The cross-range resolution  $\delta_c$  of the resulting SAR image after azimuth-compression is [8]

$$\delta_c = \frac{\lambda_c}{2L_{sa}} r_0, \quad (8)$$

where  $\lambda_c$  is the wavelength at the chirp center frequency. The expression (8) gives the distance between the main lobe peak and first null, whose position is difficult to determine in noisy measurements. Instead we use the half-power main lobe width

$$\delta_{c,3\text{dB}} = 0.88448 \delta_c \quad (9)$$

to determine the achieved resolution, where the constant factor is due to the implicit rectangular window used during azimuth compression [9].

Parameter	Symbol	Value
Start frequency	$f_0$	76 GHz
Modulation bandwidth	$B$	4 GHz
Chirp duration	$T_c$	180 $\mu$ s
Chirp repetition interval	$T_r$	200 $\mu$ s
Chirps per frame	$N_c$	256
Frame repetition interval	$T_f$	52 ms
Baseband sample rate	$f_s$	977 kHz
Number of transmit channels	$N_T$	4
Number of receive channels	$N_R$	4

**Table 1** Radar waveform parameters.

The integration gain  $G_{\text{int}}$  describes the SNR increase in the SAR image achieved by coherent processing. When integrating  $N_f$  samples, the integration gain can be expressed as [7]

$$G_{\text{int}} = N_f^\alpha. \quad (10)$$

The exponent  $\alpha$  is a measure of the integration efficiency. In the case of coherent integration  $\alpha = 1$ . In case of non-coherent integration the integration efficiency is reduced such that  $0.5 \leq \alpha < 1$  [7].

### 3 Experimental setup

The experimental setup consists of four chirp-sequence FMCW MIMO radar sensors operating between 76 GHz and 81 GHz which is the frequency range defined by ETSI for automotive radar applications [10, 11]. **Table 1** summarizes the important waveform parameters. The radar sensors are mounted onto a remote controlled mobile robot facing outward and perpendicular to the direction of movement. This enables SAR imaging of the surrounding scene. In addition to the radar sensors, an inertial measurement unit (IMU) is also attached to the center of rotation of the robot. The start of the IMU sample recording is synchronized to the first chirp sequence of a data collection run by a hardware trigger signal. The chirp-sequences of all radar sensors are synchronized via Ethernet using the precision time protocol (PTP). To avoid interference between the simultaneously operating sensors, their start frequencies were offset relative to each other by 100 MHz. Figure 1 shows the mobile robot with the mounted radar sensors used to record the dataset.

Two point-like reference targets were placed in the scene to determine the achieved SAR image resolution based on their main lobe width. The first reference target is a metal rod with a diameter of 10 mm and a length of 2 m, held vertically by a wooden block which was covered in RF absorbers to suppress strong unwanted reflections as shown in **figure 4**. The second reference target is a trihedral corner reflector (TCR) which was directly placed on top of pyramidal RF absorbers. During data collection the robot was remotely controlled to maintain a straight line path at constant speed  $v_{\text{ego}}$  while passing the reference targets. This results in the side-looking imaging geometry shown in figure 3. After data collection the robot trajectory is estimated using radar-inertial odometry (RIO) as described

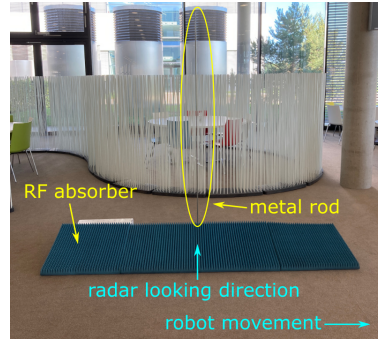


**Figure 4** Vertical metal rod (inside ellipse), RF absorber and side-looking SAR imaging geometry.

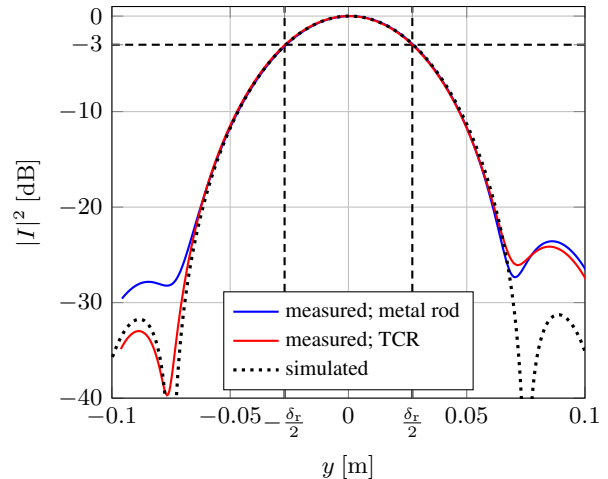


**Figure 5** Measured range peak profiles of the metal rod, trihedral corner reflector (TCR) and simulated point-target for a Hann window ( $\eta_r = 1.4381$  [9]).

in [1]. The transmit and receive channel positions  ${}_n\mathbf{p}_i$  and  ${}_n\mathbf{p}_j$  are computed from the estimated robot trajectory using the known mounting position, orientation, and antenna array geometry of each radar for every sample of the coherent processing interval. For simplicity, the SAR images used for the performance evaluation were computed from a single radar sensor only, while data from all four radars was used for trajectory estimation.

## 4 Results

### 4.1 Range resolution

**Figure 5** shows the range profile of the metal rod, trihedral corner reflector and a point-target simulation using the radar waveform parameters from table 1. The vertical dashed lines mark the half-power main lobe width as predicted by (4) for the Hann window used during range compression ( $\eta_r = 1.4381$  [9]), indicating that the computed SAR image has achieved the range resolution to be expected from the used modulation bandwidth.

### 4.2 Cross-range resolution

In order to determine the achievable cross-range resolution, the same dataset was used to compute SAR images

with successively greater synthetic aperture lengths  $L_{sa}$ . **Figures 6 and 8** show the resulting achieved cross-range resolution for the reference targets metal rod and trihedral corner reflector. Each diagram depicts data from two different measurement passes performed at robot speeds  $v_{ego}$  of 0.4 m/s and 1.0 m/s. The dashed line indicates the cross-range half-power main lobe width  $\delta_{c,3dB}$  as predicted by (9) for both scenarios.

#### 4.2.1 Metal rod

In case of the metal rod a good agreement between expected and achieved main lobe width is apparent for synthetic aperture lengths  $L_{sa} \leq 0.34$  m. Because the range of closest approach  $r_0$  for the depicted passes is 2 m, synthetic apertures longer than 0.34 m lead to an expected cross-range resolution that is smaller than the diameter of the metal rod. As the apertures become larger a splitting of the single target peak into two peaks of almost equal power can be observed. An example of this phenomenon is shown with the black dotted line in **figure 7**. This is likely caused by the scattering center on the surface of the metal rod shifting location as the radar moves past. It seems unlikely that this is caused by a creeping wave around the surface of the metal rod, as its received power is much smaller than that of the primary reflection. Furthermore, the additional propagation delay due to the small rod diameter is not resolvable at the used modulation bandwidth.

When the cross-range resolution approaches the physical target size, the point-target assumption is violated and the half-power main lobe criterion no longer seems suitable for determining the achieved cross-range resolution.

The red triangles in figure 6 show the achieved resolution for a robot speed of 0.4 m/s. One thing to note there is an outlier around  $L_{sa} = 0.14$  m, while the samples immediately preceding and following agree well with the theory. Figure 7 shows the cross-range profiles for the three circled neighboring samples in figure 6. In case of the shortest aperture  $L_{sa} = 0.102$  m, the cross-range spectrum exhibits a well defined peak. The outlier sample on the other hand has a much broader peak and a shoulder that hints at a side lobe, causing the inflated estimate for achieved cross-range resolution. The third sample with  $L_{sa} = 0.178$  m again exhibits a well defined peak, while a side lobe only about 3.5 dB below the main peak has become visible. This new side lobe is located around the same cross-range position as the shoulder in the previous profile. Because there are no targets located close to the metal rod in the experimental setup, we can conclude that this is in fact a side lobe and not an actual target reflection. Possible sources for these side lobes with significantly higher level than the  $-13.3$  dB to be expected from a rectangular window [9] will be discussed in section 4.3.

The blue triangles in figure 7 show the achieved resolution for a robot speed of 1 m/s. Similar to the lower speed case the results follow the expected resolution until a synthetic aperture length of  $L_{sa} \leq 0.34$  m. For longer synthetic apertures the deviation from the theory becomes quite large, again indicating problems related to a violation of the single point-target assumption.

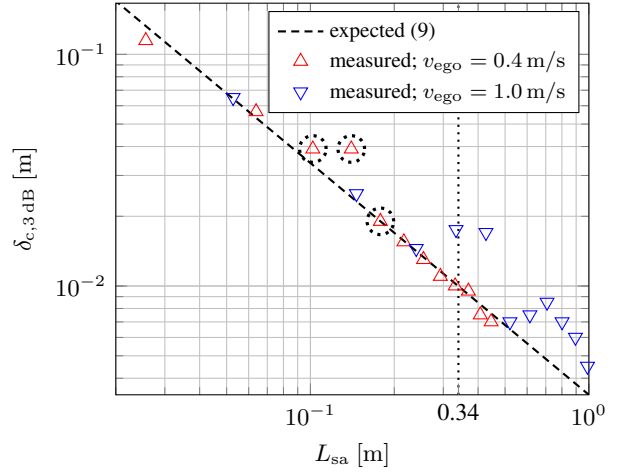


**Figure 6** Achieved cross-range half-power main lobe width for metal rod.

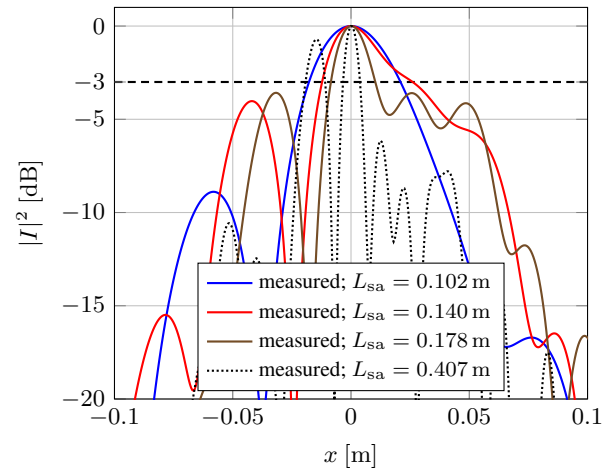


**Figure 7** Measured metal rod cross-range peak profiles for  $v_{ego} = 0.4$  m/s.

#### 4.2.2 Trihedral corner reflector

The results for the trihedral corner reflector shown in figure 8 are very similar to those of the metal rod previously discussed. For a robot speed of 0.4 m/s depicted by the magenta diamonds, a good agreement with the expected cross-range half-power main lobe width can be observed until a synthetic aperture length of  $L_{sa} = 0.26$  m. For larger aperture lengths a strong deviation from the expected main lobe width is visible. **Figure 9** shows the cross-range profile for the highlighted aperture lengths in figure 8. In case of  $L_{sa} = 0.14$  m there is a well-defined main peak, albeit with an already high side lobe level of  $-4.5$  dB. As the aperture length increases the main lobe width decreases while side lobe level increases. In case of  $L_{sa} = 0.37$  m, the main lobe appears to have split apart and the half-power main lobe width is much wider than expected.

For a robot speed of 1 m/s, a slightly longer aperture of  $L_{sa} = 0.34$  m can be synthesized before the achieved cross-range resolution no longer tracks the expected behavior. Looking at the side lobe structure in figure 9 it seems like the side lobes are the major limiting factor in our SAR imaging setup.

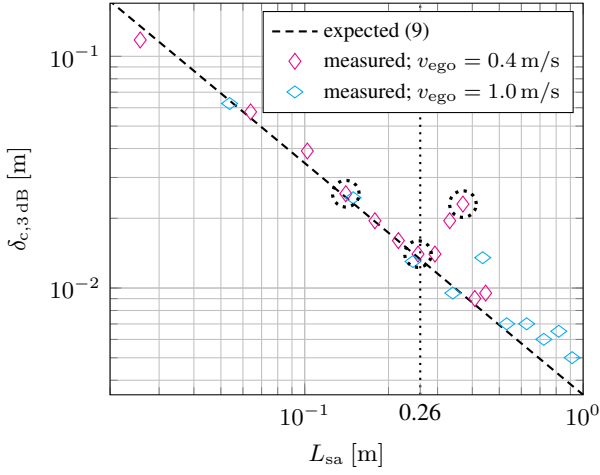


**Figure 8** Achieved cross-range half-power main lobe width for trihedral corner reflector.

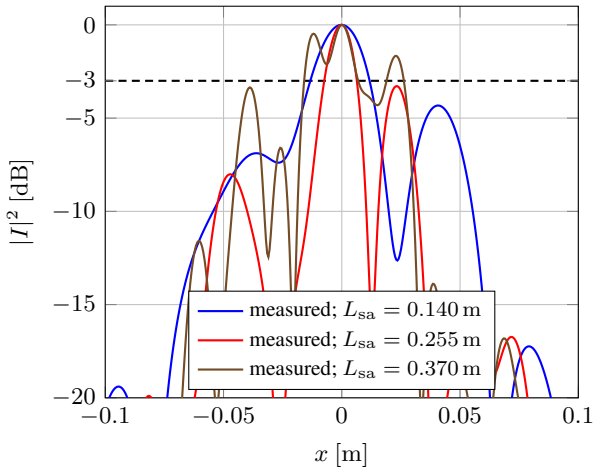


**Figure 9** Measured trihedral corner reflector cross-range peak profiles for  $v_{\text{ego}} = 0.4$  m/s.

### 4.3 Sensor vibration

The high side lobe level can be plausibly explained by low-frequency vibration of the radar sensor during data recording, which is known to cause side lobes in the Doppler-spectrum. The Doppler-spectrum resulting from a sinusoidal motion of the radar sensor during the coherent processing interval can be written in terms of an infinite series of Bessel-functions [12]. **Figure 10** shows the measured trihedral corner reflector cross-range profile for  $L_{\text{sa}} = 0.14$  m and the results of a point-target simulation with a sinusoidal vibration of the radar sensor along the  $y$ -direction (sensor boresight) during data recording. The simulated robot speed was  $v_{\text{ego}} = 0.368$  m/s to achieve the same aperture length  $L_{\text{sa}}$  as in the measurement. In order to parametrize the simulation, a single dominant vibration component was assumed to be present. The vibration frequency  $f_{\text{vib}}$  was chosen based on the expected Doppler-frequency of a target at side lobe position  $x_{\text{vib}}$

$$f_{\text{vib}} = \frac{2v_{\text{ego}}}{\lambda_c} \frac{x_{\text{vib}}}{\sqrt{x_{\text{vib}}^2 + r_0^2}}, \quad (11)$$

which for  $x_{\text{vib}} = 0.04$  m,  $r_0 = 2$  m yields  $f_{\text{vib}} = 3.83$  Hz. The vibration amplitude  $A_{\text{vib}}$  was chosen based on the side

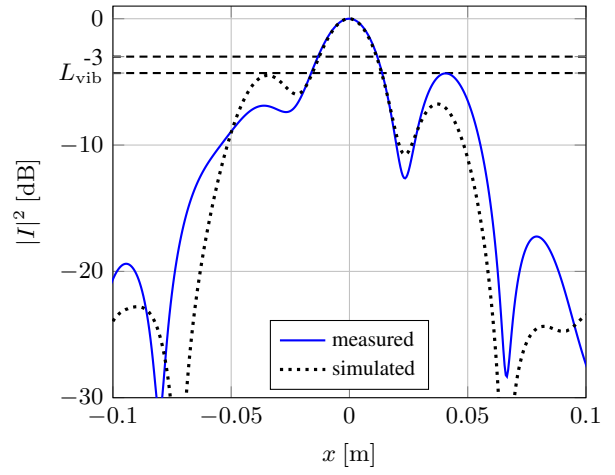


**Figure 10** Measured trihedral corner reflector and simulated point-target cross-range peak profiles for a sensor vibration with  $f_{\text{vib}} = 3.83$  Hz and  $A_{\text{vib}} = 0.319$  mm.

lobe-level  $L_{\text{vib}}$  such that it fulfills

$$L_{\text{vib}} = 20 \log_{10} \frac{J_1(a)}{J_0(a)}, \quad (12)$$

where

$$a = 2\pi \frac{2A_{\text{vib}}}{\lambda_c} \quad (13)$$

is derived in [12] and  $J_i$  is the  $i$ -th order Bessel-function of the first kind. For  $L_{\text{vib}} = -4.3$  dB this yields  $A_{\text{vib}} = 0.319$  mm. As to be expected, the highly simplified simulated vibration does not perfectly match the measurement result, it does however cause the same characteristic paired and slightly asymmetric side lobes to appear next to the main lobe. Based on this simulation it seems plausible that vibration of the radar sensor in our measurement setup causes the image degradation in terms of side lobe level. The primary focus of this paper is to quantify the performance limitations of our specific mobile robot-based SAR system. Therefore low-vibration measurement setups, such as step-motor driven linear rail, were not investigated in this study. Furthermore it was not investigated whether the vibration-induced sidelobe level could be reduced using autofocus algorithms.

### 4.4 Integration gain

**Figure 11** shows the achieved integration gain for all previously presented measurement passes as a function of the number of integrated radar frames  $N_f$ . Unsurprisingly, the real-world scenarios fall short of the theoretical maximum coherent integration gain predicted by (10), shown as a dashed line. For comparison, the integration gain of a simulated point-target scenario with a sinusoidal vibration as in section 4.3 is shown in black. The simulation results were averaged over 7 individual simulations with different starting phases. No averaging was applied to the measured results. The simulation results further support the hypothesis that even with otherwise perfect knowledge of the trajectory, vibration of the radar sensor negatively

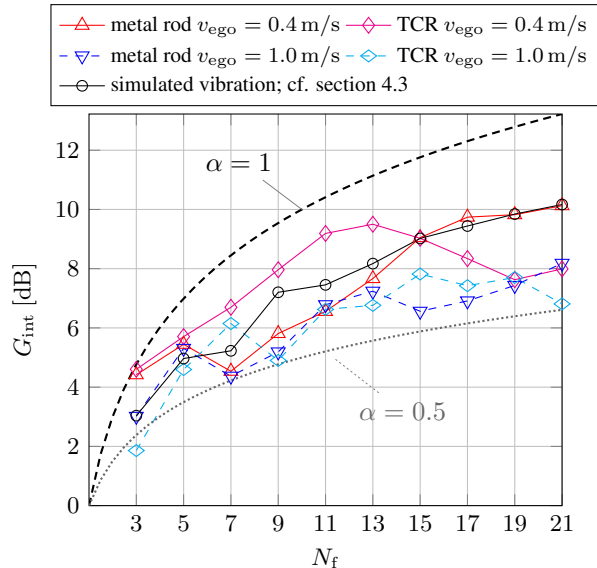


**Figure 11** Measured integration gain for different number of integrated frames. The dashed line shows the upper limit, while the gray dotted line shows the lower limit for non-coherent integration according to (10).

affects the integration gain. In case of the metal rod depicted by the triangle markers, the integration gain follows the general shape of the simulation with a similar dip at  $N_f = 7$ . The performance in terms of achieved gain is also worse than the simulation. This seems plausible, as the real measurement scenario likely includes more complex vibration patterns and unlike the simulation also suffers from errors in trajectory estimates. For the case of the trihedral corner reflector denoted by the diamonds, the integration gains drop for larger synthetic apertures, further indicating problems related to drifting trajectory estimates. Unlike non-coherent integration, the SAR image formation in (6) always operates on complex valued data. In the worst case this can lead to destructive interference of correlated target returns when trajectory estimates include sufficiently large errors. As the noise is assumed to be uncorrelated on the other hand, it should not be affected by trajectory drift during integration. The overall result is a decrease in integration gain. At a higher robot speed of  $v_{ego} = 1$  m/s, depicted by the dashed lines, the same number of integrated frames corresponds to a longer synthetic aperture. This means that the accumulated trajectory errors are also larger, explaining worse performance than in the lower speed case.

## 5 Summary

We have shown that SAR imaging using automotive radar chirp-sequence FMCW MIMO radar sensors mounted to a mobile robot based on radar-inertial odometry trajectory estimates is possible. The imaging results agree with expectations from well-known theoretical results for non-degenerate imaging cases. Vibration of the radar sensor during data collection has been identified as a major factor degrading imaging performance in terms of achievable side lobe level and integration gain. Future work will focus

on improving image quality to aid in SAR-based mapping of the indoor environment. One obvious improvement to reduce sensor vibration is to increase the mechanical stiffness of the radar mounts and avoid suspending the sensor weight from a long lever arm.

## 6 Literature

- [1] C. Doer and G. F. Trommer, "An EKF Based Approach to Radar Inertial Odometry," in *2020 IEEE International Conference on Multisensor Fusion and Integration for Intelligent Systems (MFI)*, pp. 152–159, IEEE, 2020.
- [2] Y. Almalioglu, M. Turan, C. X. Lu, N. Trigoni, and A. Markham, "Milli-RIO: Ego-Motion Estimation With Low-Cost Millimetre-Wave Radar," *IEEE Sensors Journal*, vol. 21, pp. 3314–3323, Feb. 2021.
- [3] X. Gao, S. Roy, and G. Xing, "MIMO-SAR: A Hierarchical High-Resolution Imaging Algorithm for mmWave FMCW Radar in Autonomous Driving," *IEEE Transactions on Vehicular Technology*, vol. 70, pp. 7322–7334, Aug. 2021.
- [4] T. Grebner, A. Grathwohl, P. Schoeder, V. Janoudi, and C. Waldschmidt, "Probabilistic SAR Processing for High-Resolution Mapping Using Millimeter-Wave Radar Sensors," *IEEE Transactions on Aerospace and Electronic Systems*, pp. 1–16, 2023.
- [5] F. Harrer, F. Pfeiffer, A. Löffler, T. Gisder, and E. Biebl, "Synthetic aperture radar algorithm for a global amplitude map," in *2017 14th Workshop on Positioning, Navigation and Communications (WPNC)*, pp. 1–6, IEEE, 2017.
- [6] X. Li, X. Wang, Q. Yang, and S. Fu, "Signal Processing for TDM MIMO FMCW Millimeter-Wave Radar Sensors," *IEEE Access*, vol. 9, pp. 167959–167971, 2021.
- [7] M. A. Richards, J. A. Scheer, and W. A. Holm, *Principles of Modern Radar*, vol. 1. SciTech Publishing, Inc., 2010.
- [8] A. Moreira, P. Prats-Iraola, M. Younis, G. Krieger, I. Hajnsek, and K. P. Papathanassiou, "A Tutorial on Synthetic Aperture Radar," *IEEE Geoscience and Remote Sensing Magazine*, vol. 1, pp. 6–43, Mar. 2013.
- [9] A. W. Doerry, "Catalog of Window Taper Functions for Sidelobe Control," tech. rep., Sandia National Lab.(SNL-NM), Albuquerque, NM (United States), 2017.
- [10] "ETSI EN 301 091-1 Short Range Devices; Transport and Traffic Telematics (TTT); Radar equipment operating in the 76 GHz to 77 GHz range," 2017.
- [11] "ETSI EN 302 264 Short Range Devices; Transport and Traffic Telematics (TTT); Short Range Radar equipment operating in the 77 GHz to 81 GHz band," 2017.
- [12] F. Hau, F. Baumgärtner, and M. Vossiek, "The Degradation of Automotive Radar Sensor Signals Caused by Vehicle Vibrations and Other Nonlinear Movements," *Sensors*, vol. 20, p. 6195, Oct. 2020.